POLITECNICO DI TORINO
Repository ISTITUZIONALE

Electrochemical Reduction of {CO}2 With Good Efficiency on a Nanostructured Cu-Al Catalyst

(Article begins on next page)

17 April 2024

Electrochemical Reduction of CO$_2$ With Good Efficiency on a Nanostructured Cu-Al Catalyst

Juqin Zeng[1]*, Micaela Castellino[2], Marco Fontana[2], Adriano Sacco[1], Nicolò B. D. Monti[1,2], Angelica Chiodoni[1] and Candido F. Pirri[1,2]

[1]Center for Sustainable Future Technologies @POLITO, Istituto Italiano di Tecnologia, Turin, Italy, [2]Department of Applied Science and Technology, Politecnico di Torino, Turin, Italy

Carbon monoxide (CO) and formic acid (HCOOH) are suggested to be the most convenient products from electrochemical reduction of CO$_2$ according to techno-economic analysis. To date, tremendous advances have been achieved in the development of catalysts and processes, which make this research topic even more interesting to both academic and industrial sectors. In this work, we report nanostructured Cu-Al materials that are able to convert CO$_2$ to CO and HCOOH with good efficiency. The catalysts are synthesized *via* a green microwave-assisted solvothermal route, and are composed of Cu$_2$O crystals modified by Al. In KHCO$_3$ electrolyte, these catalysts can selectively convert CO$_2$ to HCOOH and syngas with H$_2$/CO ratios between 1 and 2 approaching one unit faradaic efficiency in a wide potential range. Good current densities of 67 and 130 mA cm^{-2} are obtained at −1.0 V and −1.3 V vs. reversible hydrogen electrode (RHE), respectively. When switching the electrolyte to KOH, a significant selectivity up to 20% is observed for C$_2$H$_4$ formation, and the current densities achieve 146 and 222 mA cm^{-2} at −1.0 V and −1.3 V vs. RHE, respectively. Hence, the choice of electrolyte is critically important as that of catalyst in order to obtain targeted products at industrially relevant current densities.

Keywords: carbon dioxide utilization, electrochemistry, aluminum, copper, synthetic gas, formic acid, electrolyte

INTRODUCTION

Electrochemical conversion of CO$_2$ into valuable chemicals and fuels has attracted tremendous interest, since it possesses advantageous properties such as the utilization of green electrolytes, the high tunability of products, the potential implementation of electricity from renewable energy sources and the mild reaction conditions (Gurudayal et al., 2017; Huan et al., 2019; Sacco et al., 2020). Despite significant prospect, the electrochemical CO$_2$ reduction reaction (CO$_2$RR) encounters many challenges associated to high energy barriers, multiple parallel reactions and competitive hydrogen evolution reaction (HER) (Yin et al., 2019). Consequently, a wide range of chemicals such as carbon monoxide (CO), formate (HCOO$^-$), methane (CH$_4$), methanol (CH$_3$OH), ethane (C$_2$H$_6$), ethylene (C$_2$H$_4$) and ethanol (C$_2$H$_5$OH) is identified as the CO$_2$RR products, and the formation of H$_2$ is almost inevitable in aqueous electrolytes (Bagger et al., 2017; Zhao et al., 2018; Ren et al., 2019; Zeng et al., 2021a; Zeng et al., 2021b; Jeng et al., 2022; Zhou et al., 2022). Among these species, CO and its mixture with H$_2$ (H$_2$/CO syngas) have high relevance for the chemical industry (Nielsen et al., 2018; Zeng et al., 2020a). Particularly, several processes were already well-established for the generation of fuels and fine-chemicals from syngas (Hernández et al., 2017). Formate (HCOOH and HCOO$^-$) is

also an important chemical raw material for various industries such as leather, rubber, medicine, fiber. Moreover, it can be used as fuel in a direct formic acid fuel cell and as an excellent carrier of stored H$_2$ (Yu and Pickup, 2008; Eppinger and Huang, 2017). Most particularly, a techno-economic analysis suggests that the short-chain simple building-block molecules CO and HCOOH are currently the most compelling CO$_2$RR products (Bushuyev et al., 2018).

The acquisition of targeted products calls for suitable catalysts able to selectively drive the CO$_2$RR, and great efforts have been dedicated to the study of electrocatalysts in recent years (Nitopi et al., 2019; Li et al., 2022). Among the monometals, gold (Au), silver (Ag) and zinc (Zn) are selective for CO formation, while lead (Pb), mercury (Hg), indium (In), bismuth (Bi) and tin (Sn) are remarkably selective for HCOOH production (Bagger et al., 2017). Many bimetallic catalysts also have good potential to catalyze the CO$_2$RR toward desired products, since the electronic and geometric structures of these materials are highly tailorable. As widely reported, Cu-Zn (Moreno-García et al., 2018; Zeng et al., 2020b), Cu-Sb (Li et al., 2020; Zeng et al., 2022a) and Cu-Sn (Zeng et al., 2018; Yoo et al., 2020) are demonstrated to selectively produce CO, while most of Sn and Bi bimetallic materials (Hou et al., 2019; Wu et al., 2021) show good HCOOH selectivity. The most intensively studied bimetallic material system is Cu-Sn that can efficiently produce CO and HCOOH at controllable proportions by engineering the Cu/Sn ratio of the catalyst surface (Rabiee et al., 2020). Cu-Ag materials are another class of bimetallic catalysts that are widely reported for CO$_2$RR. Herzog et al. showed a catalyst with 5 at% Ag on Cu$_2$O nanocubes, achieving a two-fold increase in the Faradaic efficiency for C$_{2+}$ liquid products (30% at −1.0 V$_{RHE}$) (Herzog et al., 2021). Y.C. Li et al. developed a bimetallic Ag/Cu catalyst that achieved a good Faradaic efficiency of 41% toward ethanol at 250 mA cm^{-2} and −0.67 V$_{RHE}$, leading to a cathodic side (half-cell) energy efficiency of 24.7% (Li et al., 2019). On contrast, Cu-Al materials are scarcely studied for the electrochemical CO$_2$RR. Honma et al. (Iwase et al., 2022) studied two-dimensional Cu- and Al-based layered double hydroxides with different Cu/Al ratios and sheet sizes, and obtained the best CO faradaic efficiency (FE) of 42% and the highest formate selectivity of 22% at 50 mA cm^{-2} under galvanostatic conditions. Sargent et al. (Zhong et al., 2020) identified a Cu-Al catalyst using density functional theory calculations in combination with active machine learning, which efficiently reduced CO$_2$ to C$_2$H$_4$ with a high FE over 80%. Very recently, A.S. Rasouli et al. synthesized porous Ga-doped CuAl catalysts able to disrupt carbon-carbon coupling and shift the selectivity from C$_2$H$_4$ to CH$_4$ while maintaining low hydrogen evolution activity (Sedighian Rasouli et al., 2022).

Based on the literature, Cu-Al materials show tremendous potential for CO$_2$RR application, while the reported performance are inconsistent, particularly in the selectivity. Inspired by these reported works, we continue to explore Cu-Al catalysts for CO$_2$RR. Various Cu-Al materials with different Cu/Al ratios were synthesized *via* one-step microwave-assisted method using copper acetate and aluminum nitrate as metal precursors and ethylene glycol as solvent. The obtained Cu-Al

TABLE 1 | Preparation of materials with various ratios of Cu and Al precursors.

Sample	Cu(CH$_3$COO)$_2$	Al(NO$_3$)$_3$·9H$_2$O
	(mg)	(mg)
Cu$_2$O	900	0
Cu$_2$O-Al-1	900	180
Cu$_2$O-Al-2	900	370
Cu$_2$O-Al-3	900	560
Cu$_2$O-Al-5	900	930
Cu$_2$O-Al-9	900	1670

catalysts show highly nanostructured surface that are rich of active sites, contributing to the CO$_2$RR at high reaction rates. An optimal Cu/Al ratio results in good selectivity for the CO$_2$RR, with a FE of 47% for HCOOH and 24.5% for CO in KHCO$_3$ electrolyte. When considering syngas as target instead of CO, the current efficiency is almost 100%, with only a small amount of C$_2$H$_4$. When changing the electrolyte from KHCO$_3$ to KOH, enhanced C$_2$H$_4$ selectivity as well as electrode activity are observed.

EXPERIMENTAL

Materials
Copper acetate (Cu(CH$_3$COO)$_2$, 99.9%), aluminum nitrate (Al(NO$_3$)$_3$·9H$_2$O, 98%), potassium bicarbonate (KHCO$_3$, 99.7%), ethylene glycol (EG, 99.8%), Nafion® 117 solution (5 wt%) and isopropanol were purchased from Sigma-Aldrich. Unless otherwise specified, all the materials were used as received.

Synthesis of the Catalysts
The Cu-Al catalysts were fabricated through a modified microwave-assisted solvothermal route (Zeng et al., 2020a). Typically, 0.9 g of Cu(CH$_3$COO)$_2$ and a certain amount of Al(NO$_3$)$_3$·9H$_2$O were dissolved in 40 ml of EG and 5 ml of H$_2$O. Different amounts of Al(NO$_3$)$_3$·9H$_2$O were used in order to tune the Cu/Al ratios of the materials, as shown in **Table 1**. After 10 min of vigorous agitation, the mixture was transferred into a Teflon vessel (volume 100 ml). The Teflon vessel was put in a microwave oven (Milestone STARTSynth, Milestone Inc., Shelton, Connecticut) and connected to pressure and temperature probes. The mixture was irradiated for 2 min at 900 W (T$_{Max.}$ = 220°C) and then was cooled to ambient temperature. The precipitate was separated by centrifuge and washed twice with H$_2$O and once with ethanol. The powder sample was finally obtained by vacuum drying at 60°C overnight. The Cu-Al samples were denoted as Cu$_2$O and Cu$_2$O-Al-x, where x equals to 1, 2, 3, 5 and 9, respectively.

Physical and Chemical Characterizations of the Catalysts
Field emission scanning electron microscopy (FESEM, ZEISS Auriga) was used to evaluate the morphology of the catalysts. X-ray diffraction (XRD) was performed on the powder samples

by using a PANalytical X'Pert Pro instrument (Cu-Kα radiation, 40 kV and 30 mA) equipped with an X'Celerator detector. The Rietveld refinement of XRD patterns was carried out with MAUD software (Ferrari and Lutterotti, 1994). Line broadening due to crystallite size distribution and micro-strain was modeled with the "Distribution" function implemented in MAUD, coupled with either isotropic (samples Cu$_2$O-Al-1, Cu$_2$O-Al-2, Cu$_2$O-Al-5) or anisotropic (samples Cu$_2$O, Cu$_2$O-Al-3, Cu$_2$O-Al-9) size-strain model developed by N. C. Popa (Popa, 1998). The contribution to line broadening by the X-ray diffractometer was determined by refining the XRD pattern of the LaB6 NIST standard sample, measured in identical conditions.

X-ray photoelectron Spectroscopy (XPS) has been performed by means of a PHI Versaprobe 5000 spectrometer (Physical Electronics, Chanhassen, MN, USA), equipped with a monochromatic Al K-alpha X-ray source (1486.6 eV), to check the composite surface chemical composition. A circular spot of 100 μm in diameter was selected to gather the photoelectron signal for both the high resolution (HR) and the survey spectra. All samples were subjected to a combined electron and Ar ion gun neutralizer system, to decrease the electrical charging effect during the analysis. The semi-quantitative atomic concentration and fitting procedures were acquired using CasaXPS 2.3.23 dedicated software (Casa Software Ltd.,Wilmslow, UK). All core-level peak energies were referenced to C1s peak at 284.5 eV and the background contribution in HR scans was subtracted by means of a Shirley function. In order to compare our results with a proper reference sample, we have also prepared a Cu metal foil by sputtering it inside the XPS apparatus with Argon ions at 2 kV for 5 minutes, to remove any native oxide from the top surface.

Preparation of the Electrodes

The preparation process plays an important role in maximizing the behaviors of the electrodes (Martinez Crespiera et al., 2016; Vankova et al., 2017). In this work, the electrodes were prepared by drop-casting the as-prepared catalyst onto a carbon paper. In a typical preparation, 10 mg of catalyst, 1.0 mg of carbon black (CB, Shawinigan Black AB50) and 90 μl of Nafion® 117 solution were well mixed with 150 μl of isopropanol. The mixture was sonicated for 30 min until a uniform slurry was obtained. The slurry was then coated onto a carbon paper (GDL, SIGRACET 28BC, SGL Technologies). The obtained electrode was dried at room temperature overnight to evaporate the solvents.

Electrochemical Tests and Product Analysis

Electrochemical impedance spectroscopy (EIS) measurements were performed in a three-electrode single-compartment cell at room temperature with a Metrohm Autolab electrochemical workstation. The working electrode was an as-prepared electrode with a geometric area of about 0.2 cm^2. A Pt wire was used as the counter electrode and Ag/AgCl (3 M Cl$^-$) as the reference. The electrolyte was a CO$_2$-saturated 0.5 M KHCO$_3$ aqueous solution

(pH 7.8). EIS measurements were performed at various potentials of −0.6, −0.8, −1.0, and −1.2 V vs. reversible hydrogen electrode (RHE) with an AC signal of 10 mV of amplitude and 10^{-2}–10^4 Hz frequency range. Unless otherwise specified, all potentials refer to RHE and are shifted according to Nernst equation: E (V vs. RHE) = E (V vs. Ag/AgCl) + E°$_{Ag/AgCl}$ + 0.059 * pH, where E (V vs. RHE) is the reported potential value, E (V vs. Ag/AgCl) is the potential value vs. reference electrode, E°$_{Ag/AgCl}$ is the standard potential of reference electrode and pH is the pH value of the electrolyte.

CO$_2$ electrolysis was carried out by applying chronoamperometric (CA) technique with a CHI760D electrochemical workstation. The comparison of various electrodes was carried out in 0.5 M KHCO$_3$ electrolyte, while the optimal electrode was further studied in 2.0 M KHCO$_3$ (pH 8.4) and 1.0 M KOH electrolyte (pH 12) in a customized three-compartment flow cell, as shown in Scheme S1 and thoroughly described in our previous work (Zeng et al., 2022a). A Ag/AgCl (1 mm, leak-free LF-1) was used as the reference electrode and inserted in the catholyte. A Pt foil (Goodfellow, 99.95%) was used as the counter electrode and immersed in the anolyte. The working electrode was a catalyst-coated carbon paper with a geometric area of 1.5 cm^2. In the case of KHCO$_3$ electrolyte, a proton exchange membrane (Nafion™ Membrane N117, Sigma-Aldrich) was used to separate the anodic and cathodic compartments. Both catholyte and anolyte were circuited at 2 ml min^{-1} during the test. A constant CO$_2$ flow of 10 ml min^{-1} was purged through the anolyte in order to maintain a constant pH. A CO$_2$ flow of 25 ml min^{-1} was maintained at the gas compartment of the cathodic side in order to deliver CO$_2$ as reactant and bring out products. When 1.0 M KOH electrolyte was used, an anion exchange membrane (Sustainion® 37–50, Dioxide materials) was employed to separate the anodic and cathodic compartments. Both catholyte and anolyte passed through the corresponding compartments at 2 ml min^{-1}. A CO$_2$ flow of 25 ml min^{-1} was maintained at the gas compartment of the cathodic side in order to supply CO$_2$ reactant and bring out products.

The potential was corrected by compensating the ohmic potential drop, of which 85% by the instrument (iR-compensation) and 15% by manual calculation. Gas-phase products were analyzed on-line by a micro gas chromatograph (μGC, Fusion®, INFICON) with two channels containing a 10 m Rt-Molsieve 5A column and an 8 m Rt-Q-Bond column, respectively. Both channels were equipped with a micro thermal conductivity detector. Liquid products were analyzed by a high-performance liquid chromatograph (Shimadzu HPLC) with a UV-Vis Detector set at 210 nm by using a ReproGel (300 mm × 8 mm) column, with 9.0 mM H$_2$SO$_4$ (flow rate of 1.0 ml min^{-1}) as mobile phase.

The FE for each product was calculated by dividing the charge needed to produce the actual determined amount of this product by the total charge consumed during a corresponding reduction period, as shown in **Eq. 1**:
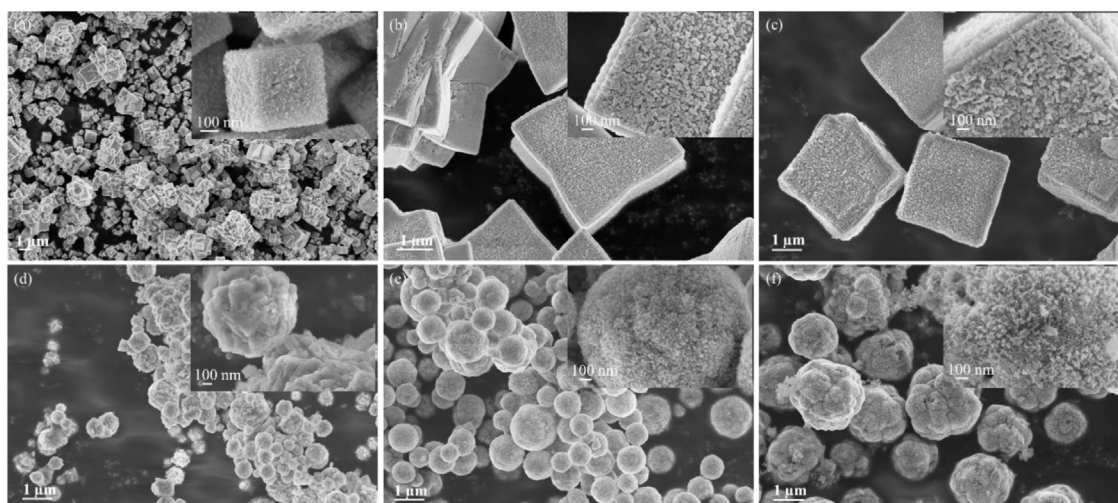
$$FE = \frac{nNF}{Q} \qquad (1)$$

FIGURE 1 | FESEM images of Cu$_2$O-Al-x samples. **(A)** Cu$_2$O; **(B)** Cu$_2$O-Al-1; **(C)** Cu$_2$O-Al-2; **(D)** Cu$_2$O-Al-3; **(E)** Cu$_2$O-Al-5 and **(F)** Cu$_2$O-Al-9.

where N is the amount of a detected product (number of moles, mol); n is the number of electrons required to obtain 1 molecule of this product ($n = 2$ for CO, HCOOH and H$_2$ formation, $n = 12$ for C$_2$H$_4$); F is the Faraday constant (96485 C mol^{-1}); Q is the total charge passed through the system recorded during electrolysis (coulombs, C).

The production rate of a product (mmol h^{-1} cm^{-2}) was calculated through **Eq. 2**:

$$Production\,rate = \frac{j_{total}*FE*t}{nF} \qquad (2)$$

where FE is the faradaic efficiency for the specific product, j_{total} is the total geometric current density of the electrode, t is a constant of 3600 and F is the Faraday constant (96485 C mol^{-1}).

RESULTS AND DISCUSSION

Physical/Chemical Properties of Cu$_2$O-Al-X Samples

Figure 1 shows the morphology of the as-prepared samples. The Cu$_2$O sample consists of submicrometric cubic and micrometric polyhedral aggregates within a size range of 0.3–0.7 μm with irregular external surface populated by nanoplatelets (**Figure 1A** and inset of **Figure 1A**). With the addition of lower amounts of Al (samples Cu$_2$O-Al-1 and Cu$_2$O-Al-2), the size of the particles increases to 2.5–3.5 μm, while the cubic morphology with nanostructured external surface is retained (**Figures 1B,C**). The addition of high amounts of Al shows a remarkable effect on the morphology of samples Cu$_2$O-Al-3, Cu$_2$O-Al-5 and Cu$_2$O-Al-9: micrometric spheres with variable size distribution (**Figures 1D–F**) are formed and each sphere consists of loosely packed nano-sized particles (inset of **Figures 1D–F**). The aggregates increases in size as raising the amount of Al precursor for sample Cu$_2$O-Al-3, Cu$_2$O-Al-5 and Cu$_2$O-Al-9.

TABLE 2 | Element distribution by EDX on various Cu$_2$O-Al-x samples.

Sample	C	O	Al	Cu	Cu/Al	Al[a]
	(at.%)	(at.%)	(at.%)	(at.%)	(at./at.)	(wt.%)
Cu$_2$O-Al-1	33.6	26.8	0.7	38.9	56	0.4
Cu$_2$O-Al-2	38.6	25.9	0.9	34.6	39	0.9
Cu$_2$O-Al-3	21.1	29.5	2.8	46.6	16	2.5
Cu$_2$O-Al-5	17.0	35.7	2.8	44.4	16	3.8
Cu$_2$O-Al-9	49.7	26.7	1.2	22.4	19	7.1

[a]The weight percentage of Al is quantified by ICP.

The Cu$_2$O-Al-3 shows an aggregate size of 0.3–0.7 μm, and it increases to 0.7–1.6 μm for Cu$_2$O-Al-5 and 1.6–2.3 μm for Cu$_2$O-Al-9 sample. It is worth to note that the effect of Al addition on the morphology is similar with that of the doping with Sn (Deng et al., 2015) and Sb (Zeng et al., 2022a). The reason of this phenomenon is not clearly stated in the literature and remains unclear in this study. Further work is needed in order to clarify this point.

EDX analysis was performed to roughly evaluate the chemical composition of the materials. As listed in **Table 2**, C, O, Cu and Al are the main detected elements. The C signal is produced by the carbon tape used for FESEM sample preparation and by the adventitious carbon contamination. The atomic ratio of Cu and Al decreases as lowering that of their salts in the precursor solution from Cu$_2$O-Al-1 to Cu$_2$O-Al-3, while it does not decrease for Cu$_2$O-Al-5 and Cu$_2$O-Al-9 when further increasing the Al salt in the precursor solution. However, ICP analysis shows a gradual increase in the weight percentage of Al in the samples with increasing the Al salt in the precursor solution. This outcome indicates the inhomogeneity of the materials, that is, a minor phase rich of Al could exist. This hypothesis is confirmed by detailed FESEM and EDX analysis. As shown in Figure S1, scarce and large agglomerations are present in the
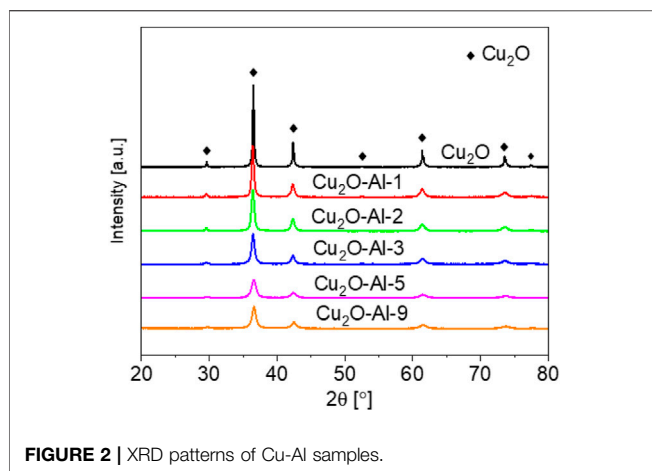
FIGURE 2 | XRD patterns of Cu-Al samples.

TABLE 3 | Refined parameters of microstructure: lattice constant α, crystallite size and micro-strain.

Sample	α (Å)	Size (nm)	Micro-strain (*10^{-4})
Cu$_2$O	4.2660	92–146	2.0–2.4
Cu$_2$O-Al-1	4.2677	132	1.0
Cu$_2$O-Al-2	4.2686	91	19
Cu$_2$O-Al-3	4.2630	84–132	19–24
Cu$_2$O-Al-5	4.2699	41	32
Cu$_2$O-Al-9	4.2693	12–37	9.8–10

Cu$_2$O-Al-5 and Cu$_2$O-Al-9 samples, and they are mainly composed of Al and O with low Cu percentages.

To identify the crystalline phase compositions of the materials, XRD analysis has been employed on the powder samples. As shown in **Figure 2**, all peaks are associated to the (110), (111), (200), (211), (220), (311) and (222) planes of Cu$_2$O with a cubic structure (Crystallography Open Database ID: 9007497, cubic unit cell, lattice constant a = 4.2685 Å, P n -3 m space group) for all samples. It is interesting to notice that no Al-containing crystalline phase is identified, suggesting that Al could be successfully incorporated in the Cu$_2$O crystalline structure. Moreover, there is no significant contribution from amorphous phases, since the XRD patterns do not show the typical large bumps of amorphous materials (Bates et al., 2006).

Further information on the microstructure is obtained by the Rietveld method, which allows the estimation of crystallite size and micro-strain contributions to the XRD pattern. The refined parameters are provided in **Table 3**, while the Rietveld refinement plots are shown in the Supporting Information (**Supplementary Figure S2**). Concerning the lattice constant of the cubic unit cell, it does not show significant deviation with respect to the reference value of a = 4.2685 Å, since for any sample the variation is comparable to 0.1% or lower and there is no correlation with the Al content. The estimated crystallite size, however, shows clear correlation with the Al content: a higher amount of Al precursor ratio results in a smaller average crystallite size. This effect is particularly noticeable for samples Cu$_2$O-Al-5 and

Cu$_2$O-Al-9, which exhibit average crystallite sizes lower than 50 nm. Regarding the micro-strain, moderate values in the 10^{-4}–10^{-3} range are estimated, which are expected for defective nanostructured materials (Handoko et al., 2016; Andrade et al., 2017). No correlation is found between Al-precursor content and micro-strain values.

XPS analysis has been conducted on selected Cu$_2$O-Al-x samples (Cu$_2$O-Al-1, Cu$_2$O-Al-3 and Cu$_2$O-Al-5) and bare Cu$_2$O powder. A Cu metallic foil has also been analyzed, in order to obtain reference spectra to be compared with those of the homemade materials. Cu XPS signals have always represented a crucial and quite tricky set of data to be deconvoluted properly, since different Cu oxidation states are not simply recognizable and distinguishable, especially Cu(I) and Cu(0). When Cu(II) is present, a well-defined satellite region appears in the range (940–950) eV, so the Cu(II) is clearly detectable. When a mix of oxidation states exists, an attenuation of the Cu(II) satellite is clearly evident, according to the relative percentage of each species. To have much more information, necessary to obtain a complete scheme of the Cu chemical shifts, we must acquire not only the Cu2p doublet region (see **Figure 3A**), but also the CuLMM Auger peak (**Figure 3C**) and the valence band (VB) region as well (**Figure 3D**). The Auger peak will add new information which can be coupled with the Cu2p doublet position in order to calculate the modified Auger Parameter (Biesinger, 2017), which allows us to distinguish between Cu(0) and Cu(I), among other species and compounds. This latter distinction can be further confirmed by analyzing the shape of the VB region, which extends almost from 0 to 14 eV (Fernandez et al., 2020). Since Al2p signal is completely covered by Cu3p doublet (see **Figure 3B**), also this latter region has been acquired to get information about Cu and Al at the same time (Al2s signal is completely covered instead by Cu3s peak, region not reported). If we start by looking at the Cu2p doublet region (**Figure 3A**), we can see that while Cu$_2$O sample shows a typical spectrum mainly due to Cu(I) with a small amount of Cu(II), which can be inferred by the small satellite peak at 540–545 eV, Cu$_2$O-Al-x samples show a lower satellite, which means that a lower percentage of Cu(II) is expected. To be more precise, we can calculate the ratio between Cu(II) and (Cu(I)+Cu(0)) thanks to the equations presented by M. Biesinger (Biesinger, 2017). The results obtained are reported in **Table 4**. There is a trend starting from the bare Cu$_2$O sample, which possesses the highest amount of Cu(II) = 17%, while samples with Al, at different %, show the same amount of Cu(II) = 8%. Just to compare, also the metal sample has been included, showing a Cu(II) = 0%. If we look instead at the Full Width at Half Maximum (FWHM) parameter for Cu2p$_{3/2}$ peak (see **Table 4**), we can observe an enlargement of the peak starting from 1.22 eV for bare Cu$_2$O till 1.70 eV for Cu$_2$O-Al-5. Since the FWHM increase is not related to the appearance of a new component due to a new oxidation state, as verified with the ratio calculated just above, this means that the inclusion of Al atoms in the Cu-based matrix leads to a more "disordered" material, which is reflected in the related peak broadening. Something similar happens in the Cu3p region (see **Figure 3B**) where we can clearly see not only a broadening of
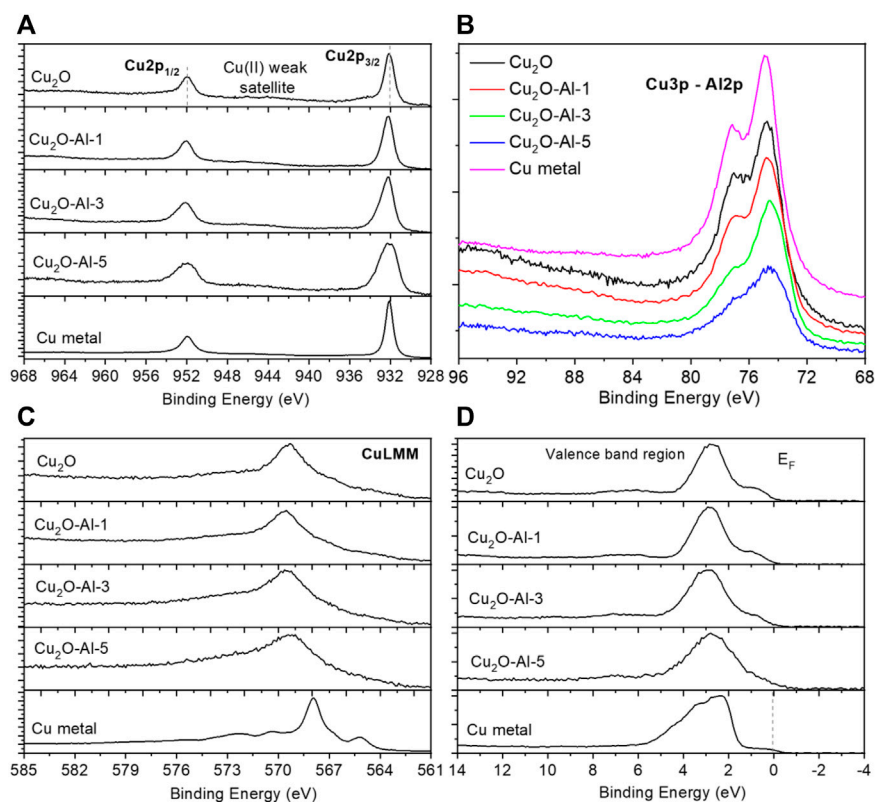
FIGURE 3 | XPS spectra of **(A)** Cu2p doublet, **(B)** Cu3p and overlapping Al2p region, **(C)** CuLMM Auger peaks and **(D)** valence band regions (E_F stands for Fermi Energy level) for Cu_2O, Cu_2O-Al-1/3/5 and Cu metal reference samples.

TABLE 4 | XPS parameters related to Cu2p3/2 peak FWHM, Cu(II)/Cu(I)+Cu(0) ratio, Modified Auger Parameters calculated for this work and reference values from the literature (Biesinger, 2017) and correlated average oxidation state for Cu, for samples Cu_2O, Cu_2O-Al-1/3/5 and Cu metal reference.

Sample	Cu2p$_{3/2}$ FWHM (eV)	Cu(II)/Cu(I)+Cu(0) (%)	Modified auger parameter (eV) [this work]	Modified auger parameter (eV) (Biesinger, 2017)	Average oxidation state (Biesinger, 2017)
Cu_2O	1.22	17/83	1849.5	1849.2	Cu(I)
Cu_2O-Al-1	1.27	8/92	1849.3	1849.2	Cu(I)
Cu_2O-Al-3	1.48	8/92	1849.2	1849.2	Cu(I)
Cu_2O-Al-5	1.70	8/92	1849.5	1849.2	Cu(I)
Cu metal ref	0.97	0/100	1851.5	1851.2	Cu(0)

the Cu3p doublet according to the Al content increase, but also the loss of the doublet split (which is visible in the Cu metal reference curve) due to the overlapping between the Cu3p and the underneath Al2p doublet in the region of 72–76 eV.

We can add another tile to this puzzle by looking at the CuLMM Auger region (**Figure 3C**), in which we can appreciate the fact that the peak maximum remains constant in its position in all the Cu(I) containing samples (Cu_2O and Cu_2O-Al-x), while it changes dramatically when we deal with the Cu metal reference. By calculating and comparing the Modified Auger Parameters for our samples with reference in the literature (Biesinger, 2017), as reported in **Table 4**, we have a further confirmation that the average oxidation state for Cu_2O and Cu_2O-Al-x samples is

always Cu(I), while the parameter changes, as expected, for the reference metal sample. A last and final check can be done by looking at the VB region, by comparing firstly the Cu_2O and the Cu metal curves, as reported by V. Fernandez et al. (Fernandez et al., 2020), since the shape of this region is completely different for this two oxidation state (see **Figure 3D**). The addition of Al atoms creates a change in the VB region which causes the loss of the well-defined step in 0–2 eV region due to the overlap of Al contribution, which possesses a valence band curve that extends from 0 to 10 eV (Snijders et al., 2002). Concisely, all investigated Cu_2O-Al-x samples show similar chemical compositions except the different Al percentages on the surface.
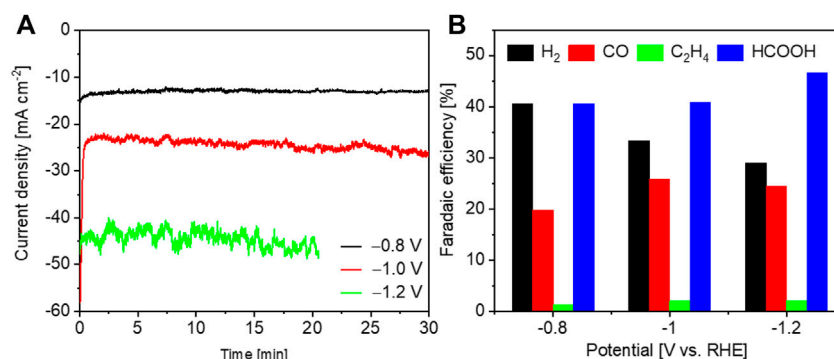
FIGURE 4 | CO_2 electrolysis on Cu_2O-Al-3 at various potentials in 0.5 M $KHCO_3$. **(A)** CA curves and **(B)** faradaic efficiencies.
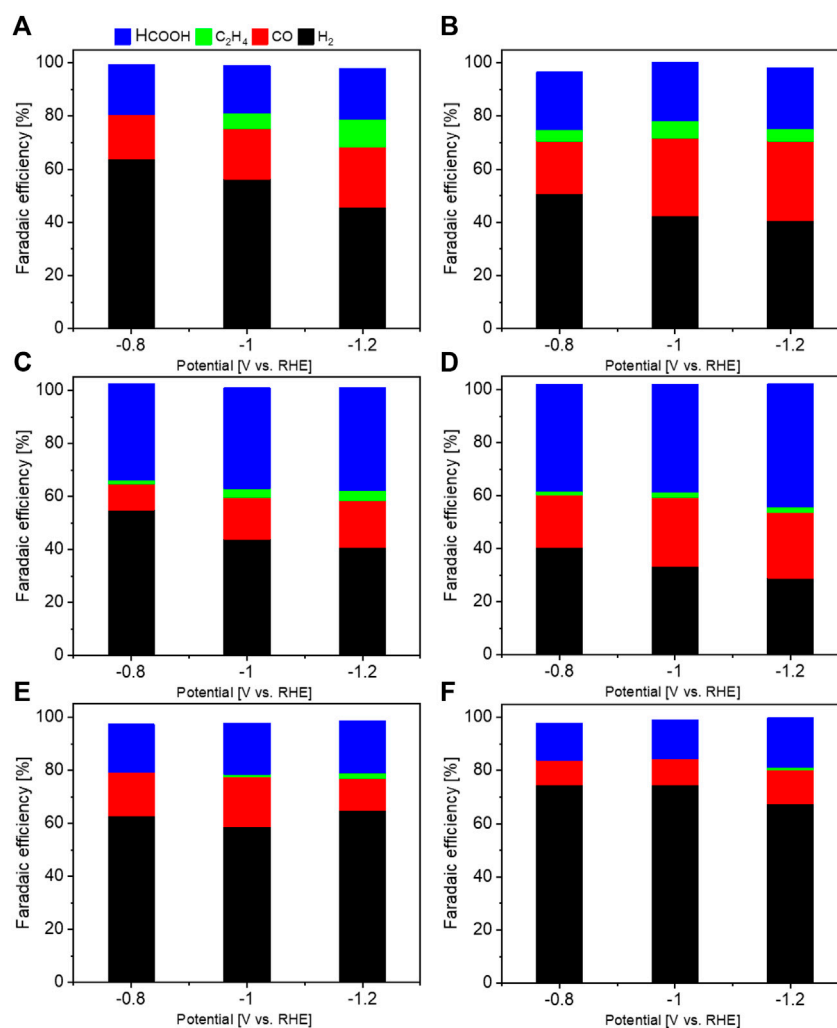

FIGURE 5 | Comparison of the selectivity of different electrodes at various potentials in 0.5 M $KHCO_3$: **(A)** Cu_2O; **(B)** Cu_2O-Al-1; **(C)** Cu_2O-Al-2; **(D)** Cu_2O-Al-3; **(E)** Cu_2O-Al-5 and **(F)** Cu_2O-Al-9.
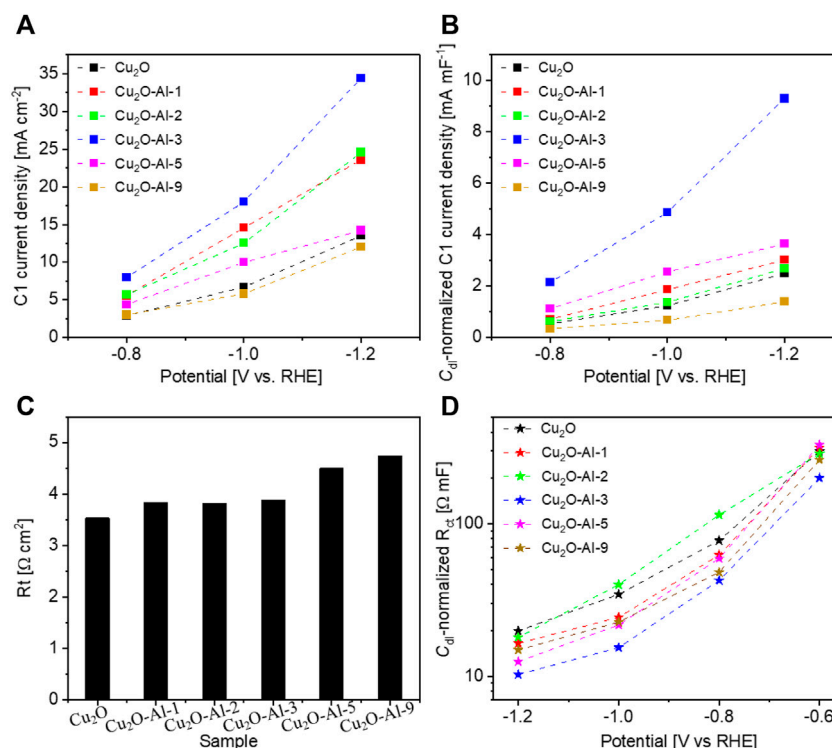
FIGURE 6 | Comparison of various electrodes: **(A)** geometric current density devoted to C1 products; **(B)** C_{dl}-normalized current density for C1 products; **(C)** Charge transport resistance and **(D)** C_{dl}-normalized charge transfer resistance.

Electrochemical Measurements and Product Analysis

CO_2 electrolysis was firstly compared on various Cu$_2$O-Al-x materials in 0.5 M KHCO$_3$ electrolyte. **Figure 4A** reports, as an example, the CA curves at different potentials for Cu$_2$O-Al-3 material. Similar curves were obtained for all other electrodes. The current density increases with raising the overpotential, and its oscillation becomes more significant as lowering the potential due to the formation of more gas products. From **Figure 4B**, it is noticed that CO and HCOOH are the main CO_2RR products together with a small amount of C_2H_4 (FE < 2.1%). The ratio of H_2/CO varies from 1.1 to 2.0 at the investigated potentials, indicating that this syngas is potentially utilizable for the methanol synthesis (Hernández et al., 2017).

Figure 5 compares the selectivity for main products at different electrodes at various potentials in 0.5 M KHCO$_3$. As shown in **Figure 5A**, Cu$_2$O has moderate selectivity for the CO_2RR, and mainly produces CO (FE 16–23%) and HCOOH (FE ~19%) with a lower amount of C_2H_4 (FE 5–10%). The modest addition of Al slightly promotes the CO_2RR against the HER on the Cu$_2$O electrode (in **Figures 5B–D**), while further introduction of Al leads to a gradual decrease of CO_2RR selectivity (**Figures 5E,F**). The selectivity for C_2H_4 production is suppressed on all Cu$_2$O-Al samples with respect to that on Cu$_2$O electrode, remaining below 2.1%. This outcome is in good agreement with the results reported by Honma et al. (Iwase et al., 2022),

while it is inconsistent with those observed by Sargent et al. (Zhong et al., 2020). Honma et al. synthesized two-dimensional Cu- and Al-based layered double hydroxides (Cu–Al/LDHs) using a simple co-precipitation method employing sodium carbonate solutions with different pH and synthesis temperatures. The elemental ratio of Cu and Al was between 1 and 3, and the sheet size was controlled. They found that both sheet size and Cu/Al ratio influence the CO_2RR selectivity. Sargent et al. prepared de-alloyed Cu-Al aggregates in micro scale on carbon papers, with the molar concentrations of Al on surfaces between 4.5% and 25%. They highlighted the importance of electrolyte-optimization strategy for multi-carbon production *via* CO_2 electroreduction. Hence, in these two papers, they used different techniques to prepare Cu-Al materials with different properties, showing distinct performance for CO_2RR. This outcome could be related to the Cu/Al ratio, morphology or test conditions. In our work, the Cu-Al materials were prepared with the same method through a microwave-assisted solvothermal route. The Cu$_2$O-Al-3, Cu$_2$O-Al-5 and Cu$_2$O-Al-9 samples show a similar surface Cu/Al ratio but different particle sizes. The Cu$_2$O-Al-3 performs better than the other two, and this could be attributed to its smaller size. Cu$_2$O, Cu$_2$O-Al-1 and Cu$_2$O-Al-2 show similar cubic morphology but with very different surface Cu/Al ratios. With increase in Al content, the CO_2RR selectivity is enhanced. Hence, both the Al content and particle size influence the performance of the catalysts. The total geometric current density (j_{total}) of various electrode at different
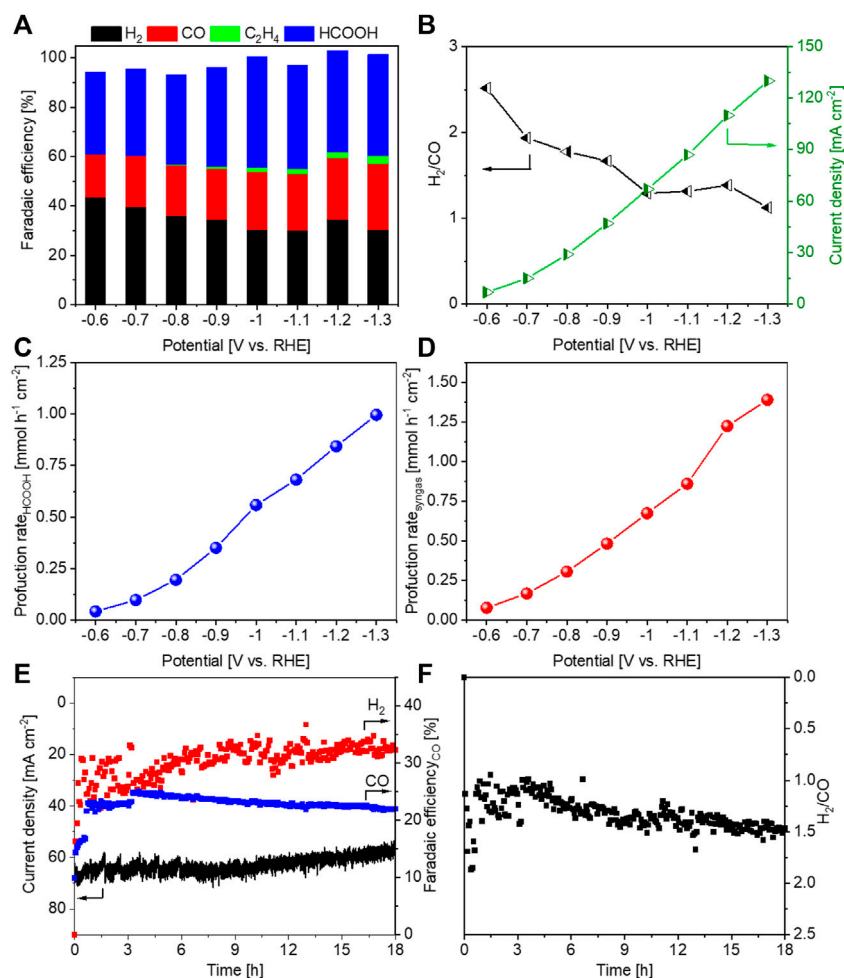
FIGURE 7 | Sample Cu$_2$O-Al-3 tested in a flow cell with 2.0 M KHCO$_3$ electrolyte. **(A)** FE values for main products, **(B)** H$_2$/CO ratios of syngas and geometric current densities, **(C)** production rate of HCOOH, **(D)** production rate of syngas, **(E)** a stability test and **(F)** H$_2$/CO ratios of syngas during the stability test.
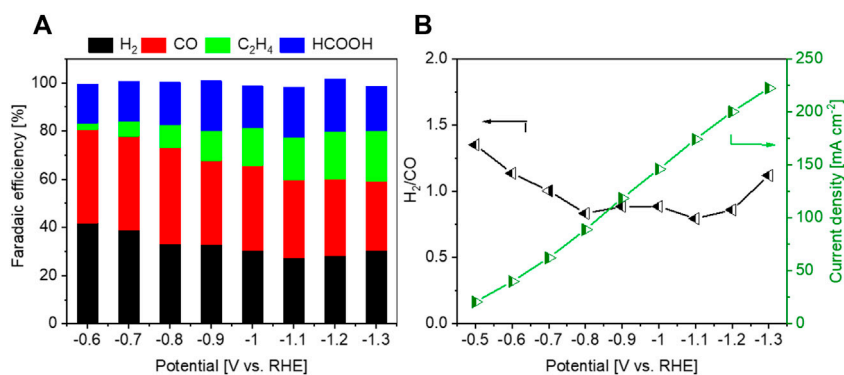

FIGURE 8 | Sample Cu$_2$O-Al-3 tested in a flow cell with 1.0 M KOH electrolyte. **(A)** FE values for main products, **(B)** H$_2$/CO ratios of syngas and geometric current densities.

potentials are shown in **Supplementary Figure S3**. All Cu$_2$O-Al-x samples show similar j_{total} at each potential, which is much higher than the one obtained on Cu$_2$O electrode at the same potential.

In order to understand better the catalytic performance of various catalysts, the geometric current density devoted to C1 products (CO and HCOOH, j_{C1}) is compared in **Figure 6A**. Similar with the trend of j_{total}, the j_{C1} is enhanced with adding a small amount of Al, peaking at the Cu$_2$O-Al-3 electrode, and then decreases with further raising the Al percentage. To elucidate the intrinsic activity of the catalysts, the current should be normalized by the electrochemically active surface area (ECSA). The ECSA represents one of the most important properties of an electrode in the electrocatalysis. Besides cyclic voltammetry (CV), EIS is considered another powerful technique to determine the ECSA of an electrode (Reid et al., 2013). For this purpose, EIS has been performed on the Cu$_2$O and Al-modified Cu$_2$O electrodes. The impedance curves acquired on Cu$_2$O-Al-3 electrode at different potentials are reported in **Supplementary Figure S4** as an example. By fitting the EIS data through the equivalent circuit shown in the inset of **Supplementary Figure S4**, the electrical parameters, including double-layer capacitance (C_{dl}), of various electrodes are obtained. All the parameters but the charge transfer resistance are found to be independent on the applied potential, in agreement with previous studies (Zeng et al., 2021c; Lourenço et al., 2021; Zeng et al., 2022b), and are reported in **Supplementary Table S1**. Since the ECSA is considered to be proportionally associated to the double-layer capacitance C_{dl}, the intrinsic activity of various materials can be compared by investigating the C_{dl}-normalized current densities. As shown in **Figure 6B**, the Cu$_2$O-Al-3 catalysts exhibits much higher electrocatalytic activity toward the CO$_2$RR to C1 products with respect to the counterparts. This outcome could be attributed to the good electrical conductivity of the Cu$_2$O-Al-3 catalyst, which is inversely proportional to the transport resistance shown in **Figure 6C**, and to the low charge transfer resistance at the electrode/electrolyte interface exhibited in **Figure 6D**.

C1 products including CO and HCOOH are the main CO$_2$RR products on the Cu$_2$O-Al catalysts in KHCO$_3$ electrolyte. The mechanism study of CO$_2$RR on metal-based materials is widely studied, in combination of *in-situ* spectroscopic analyses and DFT calculations (Rosen et al., 2015; Genovese et al., 2017; Qin et al., 2018; Zhao et al., 2019). It is widely suggested that the CO$_2$RR to CO process includes four elementary reaction steps: 1) one electron transfers to CO$_2$ to form CO$_2^{*-}$; 2) one proton transfers to CO$_2^{*-}$ to obtain COOH* intermediate; 3) an electron and a proton transfer to COOH* to form CO*; 4) CO* desorbs to produce CO. Another possible pathway is supposed to include three main steps: 1) an electron coupled with a proton transfers to CO$_2$ to form COOH* intermediate; 2) another electron coupled with a proton transfers to COOH* to form CO*; 3) CO* desorbs to produce CO. The formation of formic acid generally goes through the following pathway: 1) CO$_2^{*-}$ radical anion is firstly formed *via* a one-electron transfer and bonded to the electrode surface through O atom, 2) protonation of CO$_2^{*-}$ on the carbon atom leads to the

formation of a HCOO* intermediate and 3) a second electron transfer and protonation step results in the HCOOH product.

The best-performing Cu$_2$O-Al-3 sample was further studied with 2.0 M KHCO$_3$ electrolyte. As shown in **Figure 7A**, the FE$_{HCOOH}$ ranges from 33% to 44%, and FE$_{CO}$ varies between 17% and 26% at all the investigated potentials. A syngas with H$_2$/CO ratio between 1 and 2 is formed at all potentials more negative than −0.6 V, and the current density is boosted in 2.0 M KHCO$_3$ electrolyte with respect to that in the 0.5 M one, due to the higher conductivity of the former (**Figure 7B**). In addition, a more concentrated KHCO$_3$ electrolyte leads to higher CO$_2$ availability near the active sites (Zeng et al., 2022a), thus resulting in higher reaction rate and larger current density. The production rates for HCOOH and syngas achieve 0.56 and 0.67 mmol h^{-1} cm^{-2}, respectively, at −1.0 V, and they increase up to 1.0 and 1.4 mmol h^{-1} cm^{-2}, respectively, at −1.3 V, as reported in **Figures 7C,D**.

A long-term test has been perform on the Cu$_2$O-Al-3 sample at −1.0 V with 2.0 M KHCO$_3$ electrolyte. As can be seen from **Figure 7E**, FE$_{CO}$ decreases, and FE$_{H_2}$ increases as a function of time. The current density decreases gradually during the test. Correspondingly, the H$_2$/CO ratio rises but it remains between 1 and 1.5 during all the test (**Figure 7F**). Hence, the sample shows average stability at −1.0 V during an 18-h test. The degradation for the performance could be due to the restructuring of the material (Nitopi et al., 2019) or the formation of salts on the backside of the electrode (Sedighian Rasouli et al., 2020).

It is also observed that the selectivity for C$_2$H$_4$ production remains below 3.0% in 2.0 M KHCO$_3$. Compared with the results reported by Honma et al. (Iwase et al., 2022) and by Sargent et al. (Zhong et al., 2020), it is likely that the employed electrolyte plays a vital role on the selectivity. To understand better this aspect, the Cu$_2$O-Al-3 was further tested in a flow cell with 1.0 M KOH electrolyte. As shown in **Figure 8**, the C$_2$H$_4$ selectivity is significantly enhanced at all investigated potentials, ranging from 1.6% at −0.6 V to 21.0% at −1.3 V. The FE for HCOOH remarkably decreases, while those for CO and H$_2$ as well as the H$_2$/CO ratios are insignificantly altered. Regarding the electrode activity, the geometric current density is almost doubled in the KOH electrolyte with respect to that obtained in the 2.0 M KHCO$_3$ one at each potential. These outcomes confirm the important roles of the employed electrolyte on the activity and selectivity of CO$_2$RR. The KOH electrolyte has enhanced conductivity compared to KHCO$_3$ one, due to the higher mobility of the ions, leading to higher reaction rates. Some studies also showed that surface hydroxyls offer effective sites to boost CO$_2$ adsorption *via* hydrogen bond, enhancing the CO$_2$RR activity and selectivity (Deng et al., 2019). The higher selectivity for C$_{2+}$ products in KOH is attributed to the higher pH at the electrocatalytic interface, which promotes the dimerization of *CO (Jouny et al., 2018). The herein obtained results, in agreement with those reported in literature, highlight the importance of the choice of electrolyte besides of catalysts for tuning the CO$_2$RR toward targeted products. Moreover, the CO$_2$RR performance of the Cu-Al catalyst in this work is in line with those reported in the literatures, as shown in **Supplementary Table S2**.

CONCLUSION

In this work, Cu-Al bimetallic materials with various Cu/Al ratios were synthesized and proposed for catalyzing the CO$_2$RR to HCOOH and syngas. The optimized Cu-Al catalyst achieves good selectivity and high activity for the targeted products. Most particularly, the good selectivity of HCOOH and the H$_2$/CO ratio of syngas are maintained in a wide range of applied potentials. In 2.0 M KHCO$_3$ electrolyte, the production rates for HCOOH and syngas achieve good values of 1.0 and 1.4 mmol h^{-1} cm^{-2} at -1.3 V, respectively. Both HCOOH and syngas are important C1-building blocks that are highly relevant for the chemical industry and have large market sizes. The herein proposed Cu-Al materials are prepared with a cost and time effective method, which is also environmentally friendly and energetically convenient, allowing their mass-scale production. Hence, they show good potential to be implemented in large-scale CO$_2$ electrolysis technologies for mass production of C1 chemicals. Further studies of Cu-Al in KOH electrolyte show enhanced selectivity for C$_2$H$_4$, highlighting the vital role of electrolyte in the CO$_2$RR besides catalysts.

DATA AVAILABILITY STATEMENT

The original contributions presented in the study are included in the article/**Supplementary Material**, further inquiries can be directed to the corresponding author.

AUTHOR CONTRIBUTIONS

CP contributed to the resources. JZ contributed to the conceptualization. JZ, MC, MF, AS, NM, and AC contributed to the investigations. All authors contributed to the manuscript composition.

SUPPLEMENTARY MATERIAL

The Supplementary Material for this article can be found online at: https://www.frontiersin.org/articles/10.3389/fchem.2022.931767/full#supplementary-material

REFERENCES

Andrade, A. B., Ferreira, N. S., and Valerio, M. E. G. (2017). Particle Size Effects on Structural and Optical Properties of BaF2 Nanoparticles. *RSC Adv.* 7, 26839–26848. doi:10.1039/c7ra01582h

Bagger, A., Ju, W., Varela, A. S., Strasser, P., and Rossmeisl, J. (2017). Electrochemical CO$_2$ Reduction: A Classification Problem. *ChemPhysChem* 18, 3266–3273. doi:10.1002/cphc.201700736

Bates, S., Zografi, G., Engers, D., Morris, K., Crowley, K., and Newman, A. (2006). Analysis of Amorphous and Nanocrystalline Solids from Their X-Ray Diffraction Patterns. *Pharm. Res.* 23, 2333–2349. doi:10.1007/s11095-006-9086-2

Biesinger, M. C. (2017). Advanced Analysis of Copper X-Ray Photoelectron Spectra. *Surf. Interface Anal.* 49, 1325–1334. doi:10.1002/sia.6239

Bushuyev, O. S., De Luna, P., Dinh, C. T., Tao, L., Saur, G., van de Lagemaat, J., et al. (2018). What Should We Make with CO$_2$ and How Can We Make It? *Joule* 2, 825–832. doi:10.1016/j.joule.2017.09.003

Deng, W., Zhang, L., Li, L., Chen, S., Hu, C., Zhao, Z.-J., et al. (2019). Crucial Role of Surface Hydroxyls on the Activity and Stability in Electrochemical CO$_2$ Reduction. *J. Am. Chem. Soc.* 141, 2911–2915. doi:10.1021/jacs.8b13786

Deng, X., Zhang, Q., Zhou, E., Ji, C., Huang, J., Shao, M., et al. (2015). Morphology Transformation of Cu$_2$O Sub-microstructures by Sn Doping for Enhanced Photocatalytic Properties. *J. Alloys Compd.* 649, 1124–1129. doi:10.1016/j.jallcom.2015.07.124

Eppinger, J., and Huang, K.-W. (2017). Formic Acid as a Hydrogen Energy Carrier. *ACS Energy Lett.* 2, 188–195. doi:10.1021/acsenergylett.6b00574

Fernandez, V., Kiani, D., Fairley, N., Felpin, F.-X., and Baltrusaitis, J. (2020). Curve Fitting Complex X-Ray Photoelectron Spectra of Graphite-Supported Copper Nanoparticles Using Informed Line Shapes. *Appl. Surf. Sci.* 505, 143841. doi:10.1016/j.apsusc.2019.143841

Ferrari, M., and Lutterotti, L. (1994). Method for the Simultaneous Determination of Anisotropic Residual Stresses and Texture by X-Ray Diffraction. *J. Appl. Phys.* 76, 7246–7255. doi:10.1063/1.358006

Genovese, C., Ampelli, C., Perathoner, S., and Centi, G. (2017). Mechanism of C-C Bond Formation in the Electrocatalytic Reduction of CO$_2$ to Acetic Acid. A Challenging Reaction to Use Renewable Energy with Chemistry. *Green Chem.* 19 (10), 2406–2415. doi:10.1039/c6gc03422e

Gurudayal, G., Bullock, J., Srankó, D. F., Towle, C. M., Lum, Y., Hettick, M., et al. (2017). Efficient Solar-Driven Electrochemical CO$_2$ Reduction to Hydrocarbons and Oxygenates. *Energy Environ. Sci.* 10, 2222–2230. doi:10.1039/c7ee01764b

Handoko, A. D., Ong, C. W., Huang, Y., Lee, Z. G., Lin, L., Panetti, G. B., et al. (2016). Mechanistic Insights into the Selective Electroreduction of Carbon Dioxide to Ethylene on Cu$_2$O-Derived Copper Catalysts. *J. Phys. Chem. C* 120 (36), 20058–20067. doi:10.1021/acs.jpcc.6b07128

Hernández, S., Amin Farkhondehfal, M., Sastre, F., Makkee, M., Saracco, G., and Russo, N. (2017). Syngas Production from Electrochemical Reduction of CO$_2$: Current Status and Prospective implementation. *Green Chem.* 19, 2326–2346. doi:10.1039/c7gc00398f

Herzog, A., Bergmann, A., Jeon, H. S., Timoshenko, J., Kühl, S., Rettenmaier, C., et al. (2021). Operando Investigation of Ag-Decorated Cu$_2$O Nanocube Catalysts with Enhanced CO$_2$ Electroreduction toward Liquid Products. *Angew. Chem. Int. Ed.* 60, 7426–7435. doi:10.1002/anie.202017070

Hou, X., Cai, Y., Zhang, D., Li, L., Zhang, X., Zhu, Z., et al. (2019). 3D Core-Shell Porous-Structured Cu@Sn Hybrid Electrodes with Unprecedented Selective CO$_2$-into-formate Electroreduction Achieving 100%. *J. Mat. Chem. A* 7 (7), 3197–3205. doi:10.1039/c8ta10650a

Huan, T. N., Dalla Corte, D. A., Lamaison, S., Karapinar, D., Lutz, L., Menguy, N., et al. (2019). Low-cost High-Efficiency System for Solar-Driven Conversion of CO$_2$ to Hydrocarbons. *Proc. Natl. Acad. Sci. U.S.A.* 116, 9735–9740. doi:10.1073/pnas.1815412116

Iwase, K., Hirano, T., and Honma, I. (2022). Copper Aluminum Layered Double Hydroxides with Different Compositions and Morphologies as Electrocatalysts for the Carbon Dioxide Reduction Reaction. *ChemSusChem* 15 (2), e202102340. doi:10.1002/cssc.202102340

Jeng, E., Qi, Z., Kashi, A. R., Hunegnaw, S., Huo, Z., Miller, J. S., et al. (2022). Scalable Gas Diffusion Electrode Fabrication for Electrochemical CO$_2$ Reduction Using Physical Vapor Deposition Methods. *ACS Appl. Mat. Interfaces* 14 (6), 7731–7740. doi:10.1021/acsami.1c17860

Jouny, M., Luc, W., and Jiao, F. (2018). High-rate Electroreduction of Carbon Monoxide to Multi-Carbon Products. *Nat. Catal.* 1, 748–755. doi:10.1038/s41929-018-0133-2

Li, X., Wu, X., Lv, X., Wang, J., and Wu, H. B. (2022). Recent Advances in Metal-Based Electrocatalysts with Hetero-Interfaces for CO$_2$ Reduction Reaction. *Chem. Catal.* 2 (2), 262–291. doi:10.1016/j.checat.2021.10.015

Li, Y., Chu, S., Shen, H., Xia, Q., Robertson, A. W., Masa, J., et al. (2020). Achieving Highly Selective Electrocatalytic CO$_2$ Reduction by Tuning CuO-Sb2O3 Nanocomposites. *ACS Sustain. Chem. Eng.* 8, 4948–4954. doi:10.1021/acssuschemeng.0c00800

Li, Y. C., Wang, Z., Yuan, T., Nam, D.-H., Luo, M., Wicks, J., et al. (2019). Binding Site Diversity Promotes CO$_2$ Electroreduction to Ethanol. *J. Am. Chem. Soc.* 141 (21), 8584–8591. doi:10.1021/jacs.9b02945

Lourenço, M. A. O., Zeng, J., Jagdale, P., Castellino, M., Sacco, A., Farkhondehfal, M. A., et al. (2021). Biochar/Zinc Oxide Composites as Effective Catalysts for Electrochemical CO₂ Reduction. *ACS Sustain. Chem. Eng.* 9 (15), 5445–5453. doi:10.1021/acssuschemeng.1c00837

Martinez Crespiera, S., Amantia, D., Knipping, E., Aucher, C., Aubouy, L., Amici, J., et al. (2016). Electrospun Pd-Doped Mesoporous Carbon Nano Fibres as Catalysts for Rechargeable Li-O2 batteries. *RSC Adv.* 6 (62), 57335–57345. doi:10.1039/c6ra09721a

Moreno-García, P., Schlegel, N., Zanetti, A., López, A. C., de Jesús Gálvez-Vázquez, M., Dutta, A., et al. (2018). Selective Electrochemical Reduction of CO₂ to CO on Zn-Based Foams Produced by Cu²⁺ and Template-Assisted Electrodeposition. *ACS Appl. Mat. Interfaces* 10, 31355–31365. doi:10.1021/acsami.8b09894

Nielsen, D. U., Hu, X.-M., Daasbjerg, K., and Skrydstrup, T. (2018). Chemically and Electrochemically Catalysed Conversion of CO₂ to CO with Follow-Up Utilization to Value-Added Chemicals. *Nat. Catal.* 1, 244–254. doi:10.1038/s41929-018-0051-3

Nitopi, S., Bertheussen, E., Scott, S. B., Liu, X., Engstfeld, A. K., Horch, S., et al. (2019). Progress and Perspectives of Electrochemical CO₂ Reduction on Copper in Aqueous Electrolyte. *Chem. Rev.* 119 (12), 7610–7672. doi:10.1021/acs.chemrev.8b00705

Popa, N. C. (1998). The (Hkl) Dependence of Diffraction-Line Broadening Caused by Strain and Size for All Laue Groups in Rietveld Refinement. *J. Appl. Cryst.* 31, 176–180. doi:10.1107/s0021889897009795

Qin, B., Li, Y., Fu, H., Wang, H., Chen, S., Liu, Z., et al. (2018). Electrochemical Reduction of CO₂ into Tunable Syngas Production by Regulating the Crystal Facets of Earth-Abundant Zn Catalyst. *ACS Appl. Mat. Interfaces* 10 (24), 20530–20539. doi:10.1021/acsami.8b04809

Rabiee, H., Zhang, X., Ge, L., Hu, S., Li, M., Smart, S., et al. (2020). Tuning the Product Selectivity of the Cu Hollow Fiber Gas Diffusion Electrode for Efficient CO₂ Reduction to Formate by Controlled Surface Sn Electrodeposition. *ACS Appl. Mat. Interfaces* 12, 21670–21681. doi:10.1021/acsami.0c03681

Reid, O. R., Saleh, F. S., and Easton, E. B. (2013). Determining Electrochemically Active Surface Area in PEM Fuel Cell Electrodes with Electrochemical Impedance Spectroscopy and its Application to Catalyst Durability. *Electrochimica Acta* 114, 278–284. doi:10.1016/j.electacta.2013.10.050

Ren, D., Gao, J., Pan, L., Wang, Z., Luo, J., Zakeeruddin, S. M., et al. (2019). Atomic Layer Deposition of ZnO on CuO Enables Selective and Efficient Electroreduction of Carbon Dioxide to Liquid Fuels. *Angew. Chem. Int. Ed.* 58, 15036–15040. doi:10.1002/anie.201909610

Rosen, J., Hutchings, G. S., Lu, Q., Rivera, S., Zhou, Y., Vlachos, D. G., et al. (2015). Mechanistic Insights into the Electrochemical Reduction of CO₂ to CO on Nanostructured Ag Surfaces. *ACS Catal.* 5 (7), 4293–4299. doi:10.1021/acscatal.5b00840

Sacco, A., Speranza, R., Savino, U., Zeng, J., Farkhondehfal, M. A., Lamberti, A., et al. (2020). An Integrated Device for the Solar-Driven Electrochemical Conversion of CO₂ to CO. *ACS Sustain. Chem. Eng.* 8, 7563–7568. doi:10.1021/acssuschemeng.0c02088

Sedighian Rasouli, A., Wang, X., Wicks, J., Dinh, C.-T., Abed, J., Wu, F.-Y., et al. (2022). Ga Doping Disrupts C-C Coupling and Promotes Methane Electroproduction on CuAl Catalysts. *Chem. Catal.* 2, 908–916. doi:10.1016/j.checat.2022.03.016

Sedighian Rasouli, A., Wang, X., Wicks, J., Lee, G., Peng, T., Li, F., et al. (2020). CO₂ Electroreduction to Methane at Production Rates Exceeding 100 mA/cm2. *ACS Sustain. Chem. Eng.* 8 (39), 14668–14673. doi:10.1021/acssuschemeng.0c03453

Snijders, P. C., Jeurgens, L. P. H., and Sloof, W. G. (2002). Structure of Thin Aluminium-Oxide Films Determined from Valence Band Spectra Measured Using XPS. *Surf. Sci.* 496, 97–109. doi:10.1016/s0039-6028(01)01591-6

Vankova, S., Francia, C., Amici, J., Zeng, J., Bodoardo, S., Penazzi, N., et al. (2017). Influence of Binders and Solvents on Stability of Ru/RuOx Nanoparticles on ITO Nanocrystals as Li-O₂ Battery Cathodes. *ChemSusChem* 10 (3), 575–586. doi:10.1002/cssc.201601301

Wu, Z., Wu, H., Cai, W., Wen, Z., Jia, B., Wang, L., et al. (2021). Engineering Bismuth-Tin Interface in Bimetallic Aerogel with a 3D Porous Structure for Highly Selective Electrocatalytic CO₂ Reduction to HCOOH. *Angew. Chem. Int. Ed.* 60 (22), 12554–12559. doi:10.1002/anie.202102832

Yin, Z., Palmore, G. T. R., and Sun, S. (2019). Electrochemical Reduction of CO2 Catalyzed by Metal Nanocatalysts. *Trends Chem.* 1, 739–750. doi:10.1016/j.trechm.2019.05.004

Yoo, C. J., Dong, W. J., Park, J. Y., Lim, J. W., Kim, S., Choi, K. S., et al. (2020). Compositional and Geometrical Effects of Bimetallic Cu-Sn Catalysts on Selective Electrochemical CO₂ Reduction to CO. *ACS Appl. Energy Mat.* 3, 4466–4473. doi:10.1021/acsaem.0c00157

Yu, X., and Pickup, P. G. (2008). Recent Advances in Direct Formic Acid Fuel Cells (DFAFC). *J. Power Sources* 182, 124–132. doi:10.1016/j.jpowsour.2008.03.075

Zeng, J., Bejtka, K., Di Martino, G., Sacco, A., Castellino, M., Re Fiorentin, M., et al. (2020). Microwave-Assisted Synthesis of Copper-Based Electrocatalysts for Converting Carbon Dioxide to Tunable Syngas. *ChemElectroChem* 7 (1), 229–238. doi:10.1002/celc.201901730

Zeng, J., Bejtka, K., Ju, W., Castellino, M., Chiodoni, A., Sacco, A., et al. (2018). Advanced Cu-Sn Foam for Selectively Converting CO₂ to CO in Aqueous Solution. *Appl. Catal. B Environ.* 236, 475–482. doi:10.1016/j.apcatb.2018.05.056

Zeng, J., Castellino, M., Bejtka, K., Sacco, A., Di Martino, G., Farkhondehfal, M. A., et al. (2021). Facile Synthesis of Cubic Cuprous Oxide for Electrochemical Reduction of Carbon Dioxide. *J. Mat. Sci.* 56, 1255–1271. doi:10.1007/s10853-020-05278-y

Zeng, J., Fiorentin, M. R., Fontana, M., Castellino, M., Risplendi, F., Sacco, A., et al. (2022). Novel Insights into Sb-Cu Catalysts for Electrochemical Reduction of CO₂. *Appl. Catal. B Environ.* 306, 121089. doi:10.1016/j.apcatb.2022.121089

Zeng, J., Fontana, M., Castellino, M., Sacco, A., Farkhondehfal, M. A., Drago, F., et al. (2021). Efficient CO₂ Electroreduction on Tin Modified Cuprous Oxide Synthesized via a One-Pot Microwave-Assisted Route. *Catalysts* 11 (8), 907. doi:10.3390/catal11080907

Zeng, J., Fontana, M., Sacco, A., Sassone, D., and Pirri, C. F. (2022). A Study of the Effect of Electrode Composition on the Electrochemical Reduction of CO₂. *Catal. Today* 397-399, 463–474. In Press. doi:10.1016/j.cattod.2021.07.014

Zeng, J., Jagdale, P., Lourenço, M. A. O., Farkhondehfal, M. A., Sassone, D., Bartoli, M., et al. (2021). Biochar-Supported BiOx for Effective Electrosynthesis of Formic Acid from Carbon Dioxide Reduction. *Crystals* 11 (4), 363. doi:10.3390/cryst11040363

Zeng, J., Rino, T., Bejtka, K., Castellino, M., Sacco, A., Farkhondehfal, M. A., et al. (2020). Coupled Copper-Zinc Catalysts for Electrochemical Reduction of Carbon Dioxide. *ChemSusChem* 13, 4128–4139. doi:10.1002/cssc.202000971

Zhao, S., Jin, R., and Jin, R. (2018). Opportunities and Challenges in CO₂ Reduction by Gold- and Silver-Based Electrocatalysts: From Bulk Metals to Nanoparticles and Atomically Precise Nanoclusters. *ACS Energy Lett.* 3, 452–462. doi:10.1021/acsenergylett.7b01104

Zhao, S., Li, S., Guo, T., Zhang, S., Wang, J., Wu, Y., et al. (2019). Advances in Sn-Based Catalysts for Electrochemical CO₂ Reduction. *Nano-Micro Lett.* 11 (1), 62. doi:10.1007/s40820-019-0293-x

Zhong, M., Tran, K., Min, Y., Wang, C., Wang, Z., Dinh, C.-T., et al. (2020). Accelerated Discovery of CO₂ Electrocatalysts Using Active Machine Learning. *Nature* 581, 178–183. doi:10.1038/s41586-020-2242-8

Zhou, X., Shan, J., Chen, L., Xia, B. Y., Ling, T., Duan, J., et al. (2022). Stabilizing Cu²⁺ Ions by Solid Solutions to Promote CO₂ Electroreduction to Methane. *J. Am. Chem. Soc.* 144, 2079–2084. doi:10.1021/jacs.1c12212